

# Depolarized Holography with Polarization-multiplexing Metasurface - Supplementary Material

SEUNG-WOO NAM\* and YOUNGJIN KIM\*, Seoul National University, Republic of Korea

DONGYEON KIM, Seoul National University, Republic of Korea

YOONCHAN JEONG, Seoul National University, Republic of Korea

## ACM Reference Format:

Seung-Woo Nam, Youngjin Kim, Dongyeon Kim, and Yoonchan Jeong. 2023. Depolarized Holography with Polarization-multiplexing Metasurface - Supplementary Material. *ACM Trans. Graph.* 42, 6, Article 200 (December 2023), 12 pages. <https://doi.org/10.1145/3618395>

Here we note some abbreviations frequently used throughout the supplementary text.

**RCWA** : Rigorous coupled-wave analysis

**SLM** : Spatial light modulator

## S1 ADDITIONAL DETAILS ON HARDWARE

### S1.1 Polarization-multiplexing metasurface

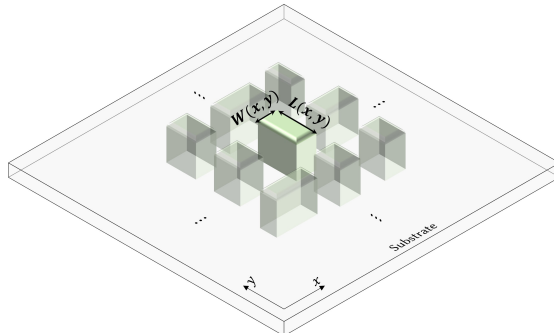


Fig. S1. Schematics of the polarization-multiplexing metasurface. Lateral dimensions along the  $x$ - and  $y$ - axes are written as  $W(x, y)$  and  $L(x, y)$ , respectively. Each nanostructure can shift the phase of  $x$ - and  $y$ - polarized light by changing the  $W$  and  $L$ .

---

\*Both authors contributed equally to this research.

---

Authors' addresses: Seung-Woo Nam, 711asd@snu.ac.kr; Youngjin Kim, ttw8592@snu.ac.kr, Seoul National University, Republic of Korea; Dongyeon Kim, Seoul National University, Republic of Korea, dongyeon93@snu.ac.kr; Yoonchan Jeong, Seoul National University, Republic of Korea, yoonchan@snu.ac.kr.

---

Permission to make digital or hard copies of all or part of this work for personal or classroom use is granted without fee provided that copies are not made or distributed for profit or commercial advantage and that copies bear this notice and the full citation on the first page. Copyrights for components of this work owned by others than the author(s) must be honored. Abstracting with credit is permitted. To copy otherwise, or republish, to post on servers or to redistribute to lists, requires prior specific permission and/or a fee. Request permissions from permissions@acm.org.

© 2023 Copyright held by the owner/author(s). Publication rights licensed to ACM.

Manuscript submitted to ACM

*Principles of independent phase modulation for orthogonal linear polarization states.* Metasurfaces are two-dimensional arrays of nano-scatterer with a subwavelength period, as shown in Figure S1. Pixel-wise variation of geometric parameters, for instance, the length and width of rectangular-shaped nanorods can change quasi-independently the effective refractive indexes along the x- and y-axis, respectively. Thus, the phase shifts occur for each orthogonal linear polarization state. This optical behavior can be represented by the Jones matrix of linearly birefringent waveplate [Arbabi et al., 2015, Mueller et al., 2017].

$$\begin{bmatrix} e^{i\phi_x} & 0 \\ 0 & e^{i\phi_y} \end{bmatrix} \quad (\text{S1})$$

*Phase modulation range of orthogonal linear polarization states.* In ideal case, the phase-shift of transmission coefficients for each orthogonal linear polarization states cover the whole  $2\pi$  range theoretically, which means the complete independent modulation of orthogonal polarization-pair. As explained in the main text, however, the fabrication constraint or the kind of dielectric material we use might pose a hurdle for the complete independent phase modulation. Figure S2 shows the actual phase cover range along with practical issues; a low refractive index of the silicon nitride with a limited height of the nanorod. Each point in the figure represents the phase values for  $t_{xx}$  and  $t_{yy}$ , respectively. Therefore, if it is possible to adjust the phase completely independently for two orthogonal polarizations, the points shown in the picture should be fully filled throughout the whole phase chart. As the wavelength of incident light increases, the range of possible values for the propagation phase scheme is reduced, assuming that the height of the nanorod is fixed. Thus, the phase modulation range at 638 nm wavelength shows much narrower than the case of 450 nm. The use of materials possessing higher refractive index such as titanium dioxide or amorphous silicon can be a simple solution to tackle with this problem. Also the realization of the sophisticated fabrication recipe enabling the higher aspect ratio is able to increase the phase-shift range, either.

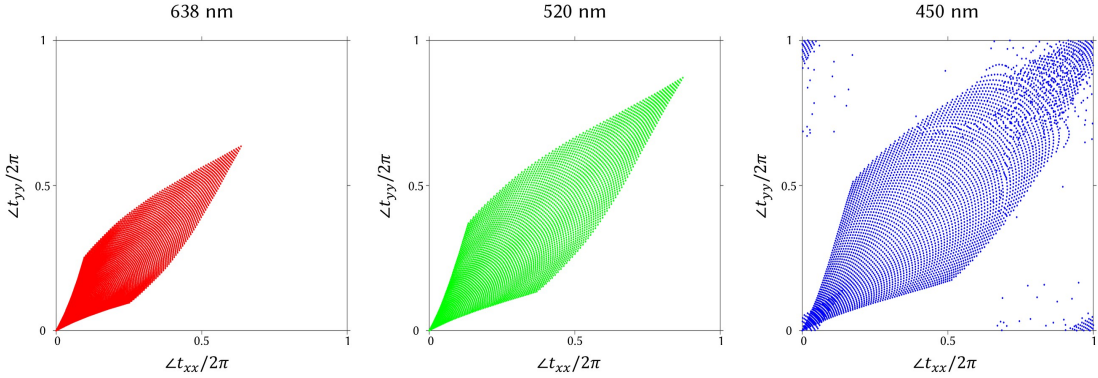


Fig. S2. Phase modulation range on the orthogonal linear polarization states at wavelengths of interest.  $\angle t_{xx}$  and  $\angle t_{yy}$  represent the phase shift of co-polarized transmission coefficient when it comes to the normal incidence of linearly polarized light. The phase shifts are normalized by  $2\pi$ .

*Proxy model fitting from the RCWA data.* Metasurface proxy model is designed from the pre-simulated transmittance of rectangular nanostructure calculated by the RCWA method. First, we have to specify several hyper-parameters that are decided by the experimental conditions. The pixel pitch of the metasurface is set to approximately 283 nm, determined under two considerations: a demagnification factor of the relay optics from SLM to metasurface and the

suppression of the unwanted resonant phenomena inside the dielectric materials for smooth-fitting. Three wavelengths of the laser source are 450, 520, and 638 nm, respectively. The refractive index ( $n$ ) and extinction coefficient ( $k$ ) of the silicon nitride layer with a deposition thickness of 800 nm. Figure S3 shows the  $n$ ,  $k$  values measured by spectroscopic ellipsometer (M2000D, Woollam). Second, given that the hyper-parameters are decided, we utilize the RCWA method to obtain transmittance libraries to be used for the proxy-model fitting. A total of six data sets on the combinations of the two phase shifts for each co-polarized transmission coefficient and the three different wavelengths, as a function of geometric parameters of the nanorod, which change from 80 to 220 nm with a 2 nm interval. For example, the phase shift of the co-polarized transmission coefficients is simulated by RCWA for every width and length value, when the x-polarized light is normally incident upon the nanostructure. Third, the discrete values of each library are fitted as a surface function using linear quadratic polynomials as explained in the main text. The phase shifts of transmitted light are also normalized by  $2\pi$ . We utilize the curve fitting toolbox from the commercial software, MATLAB. Using a linear-least-square method, the coefficients of polynomials can be obtained with a 95% confidence bound. Figure S4 shows the six proxy models against simulated values. Although we can see some outliers of the simulated data compared with the fitted functions, especially for the blue wavelength case, which is attributed to the resonant phenomena inside the dielectric materials, they are very sparse so we can neglect these exceptional points. Table 1 shows the equations and the coefficients of polynomials for all twelve proxy models.

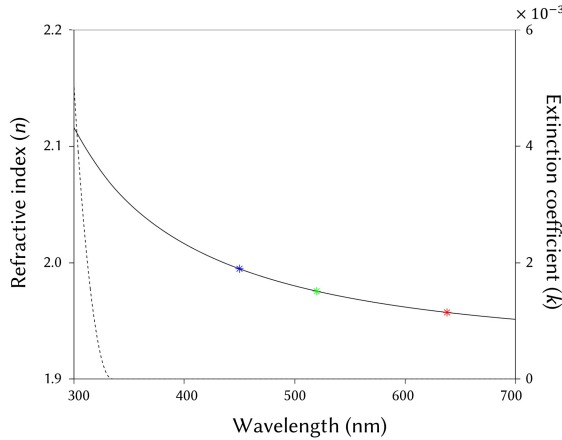


Fig. S3. Refractive index and extinction coefficient of the silicon nitride layer. The solid and dotted lines represent the refractive index (RI) and the extinction coefficient. The RI at wavelengths 450, 520, and 638 nm are marked with blue-, green-, and red-colored asterisks, which are 1.995, 1.976, and 1.957, respectively.

### S1.2 Display prototype

The holographic display prototype used for experimental validation is illustrated in Figure S5. Our prototype follows the basic structure of a conventional holographic display, with a half-wave plate (HWP) and a metasurface (MS) positioned after the  $4f$  system. Additionally, to facilitate metasurface alignment, an extra  $4f$  system is placed after the metasurface. The light from a full-color fiber-coupled laser diode (FISBA READYBeam) is collimated using a collimating lens and directed to the 8-bit SLM (HOLOEYE LETO-3) via a beam splitter (BS). Prior to the beam splitter, a HWP

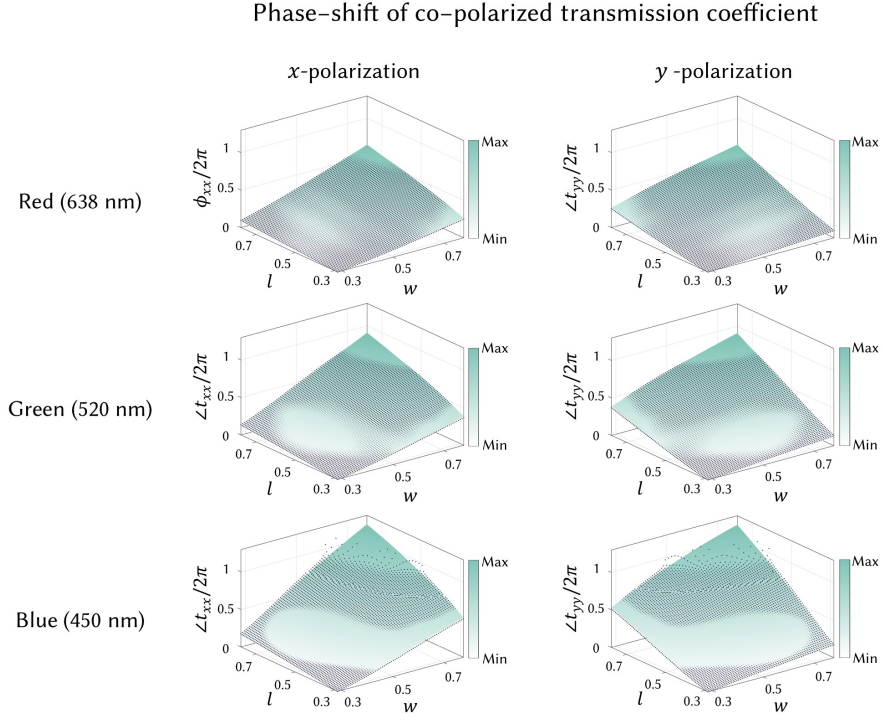


Fig. S4. Fitted surface functions and the original RCWA data.  $l$  and  $w$  are the normalized lengths and widths of the nanorod, in which the normalization factor is the pixel period of the metasurface. At each figure, the surface functions describe the proxy models and the simulated data are represented by the charcoal-colored point clouds.

Table 1. Fitted coefficients of the linear quadratic polynomials. The coefficients of  $c_{12}$ ,  $c_{21}$ , and  $c_{22}$  are set to zeros. Superscripts 'r', 'g', and 'b' correspond to red, green, and blue.  $t_{xx}$  defines the co-polarized transmission coefficient when the x-polarized light is normally incident upon the nanostructure.

Physical entity	$c_{00}$	$c_{10}$	$c_{01}$	$c_{20}$	$c_{11}$	$c_{02}$
$\phi_{xx}^r$	-0.0946	-0.1171	0.06675	0.3065	1.204	-0.2145
$\phi_{xx}^g$	-0.3072	0.3484	0.3064	0.05226	1.543	-0.4258
$\phi_{xx}^b$	-0.7156	1.366	0.8043	-0.5976	1.743	-0.8002
$\phi_{yy}^r$	-0.09458	0.06663	-0.1175	-0.2144	1.204	0.3069
$\phi_{yy}^g$	-0.3072	0.3064	0.3486	-0.4258	1.543	0.05215
$\phi_{yy}^b$	-0.7157	0.8048	1.365	-0.8004	1.742	-0.5967

and a linear polarizer (LP) are included to ensure proper polarization alignment for the SLM. The light transmitted through the SLM passes through the  $4f$  system equipped with a low-pass filtering system to eliminate high-order diffraction terms. Following the first  $4f$  system, an LP is positioned to filter out undiffracted terms, and an HWP on a

motorized rotation mount is incorporated to control the direction of linear polarization of the light from the SLM. The metasurface is mounted on 3-axis linear stages, comprising two motorized stages in the X-axis (Thorlabs LTS300/M) and Y-axis (Thorlabs Z812B), as well as a Z-axis manual stage. These stages enable precise alignment of the SLM and the metasurface, and the motorized stages enable switching between capturing images with and without the metasurface. Finally, the metasurface plane is relayed through a second  $4f$  system, and the resulting image is captured using a CCD camera (FLIR GS3-U3-51S5M-C) mounted on a motorized stage (Newport FCL100). As real images of the holograms are captured instead of virtual images with an eyepiece, the propagation distance of the hologram is calculated assuming a 50 mm eyepiece.

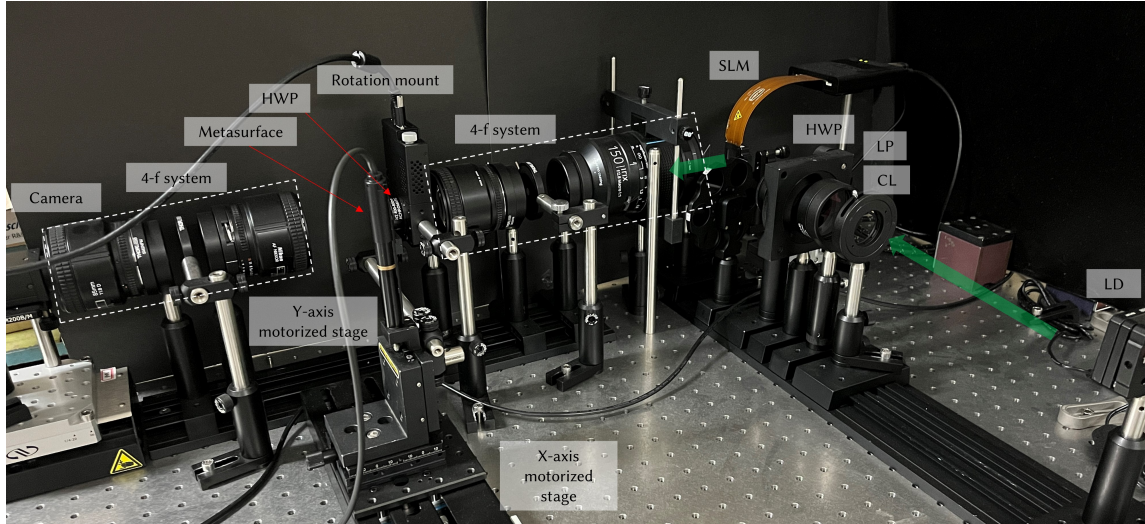


Fig. S5. Photograph of our holographic display prototype. The green arrows indicate the direction of the optical path. The optical components labeled in the photograph include laser diode (LD), SLM (spatial light modulator), collimating lens (CL), half-wave plate (HWP), linear polarizer (LP), beam splitter (BS).

### S1.3 Metasurface alignment

In Section 5.1, we discuss the utilization of the second  $4f$  system in our display prototype for aligning the metasurface and the SLM. The  $4f$  system allows us to directly capture the SLM plane and observe the positioning of both the SLM and the metasurface. Figure S6 shows an captured image of the relayed SLM plane, where a misalignment of  $30\mu\text{m}$  in both vertical and horizontal directions between the metasurface and the SLM is present. The boundary lines of the SLM and the metasurface is clearly visible, enabling manual alignment. It is worth noting that this misalignment corresponds to a shift of 10 pixels in the simulation, representing the maximum misalignment error of the noise function  $f_{\text{noise}}$  employed during metasurface optimization. Since this level of misalignment is detectable by the camera, it is evident that the misalignment error in our display prototype would be much smaller than what is simulated using the noise function  $f_{\text{noise}}$ . Therefore, we did not conduct additional calibration steps for more precise alignment and instead relied on camera-in-the-loop training for fine-tuning.

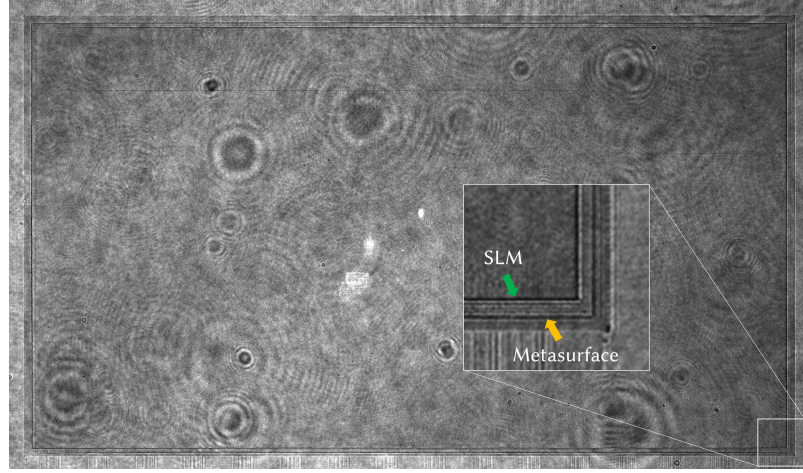


Fig. S6. The captured image shows the relayed SLM plane. In this image, a misalignment of  $30\ \mu\text{m}$  is present between the metasurface and the SLM in both the horizontal and vertical directions. The enlarged inset highlights that the boundary lines of the SLM and the metasurface are clearly visible.

## S2 DETAILS ON CAMERA-IN-THE-LOOP TRAINING

### S2.1 Propagation model

We use camera-in-the-loop (CITL) calibrated wave propagation model during CGH optimization for the experiments[Peng et al., 2020]. Our goal is to clarify the effect of the polarization-multiplexing metasurface, which is optimized in ideal simulation. Therefore, quality degradation from discrepancy between the simulation and the real-world system may weaken the effect of the metasurface in the experiment.

We combine the CNNpropCNN model proposed by Choi et al. [2022] and the all-physically interpretable model by Jang et al. [2022] in our approach. Since our model aims to accurately simulate the polarization-multiplexing phenomenon, we exclude black-box models such as CNN before the metasurface. Instead, we model the nonlinear phase response of the SLM using a multi-layer perceptron [Peng et al., 2020] and incorporate the SLM pixel crosstalk noise by convolving a  $3\times 3$  kernel with the SLM phase pattern [Jang et al., 2022]. After the SLM phase mapping through the MLP and the crosstalk kernel, we apply the complex field of the light source  $a_{\text{src}}, \phi_{\text{src}}$  and the metasurface, while taking into account the rotation angle of the half-wave plate. To account for potential misalignment between the fast axis of the HWP and the metasurface, we parameterize the rotation angle error of the HWP as  $\theta_{\text{tilt}}$ . Therefore, the Jones matrix of the HWP becomes

$$J_{\text{hwp}}(\theta; \theta_{\text{tilt}}) = \begin{bmatrix} \cos(2(\theta + \theta_{\text{tilt}})) & \sin(2(\theta + \theta_{\text{tilt}})) \\ \sin(2(\theta + \theta_{\text{tilt}})) & -\cos(2(\theta + \theta_{\text{tilt}})) \end{bmatrix}, \quad (\text{S2})$$

where  $\theta$  is the angle of the HWP for polarization rotation, with  $0^\circ$ ,  $45^\circ$ , and  $22.5^\circ$  corresponding to horizontal, vertical, and diagonal linear polarization, respectively. For simplicity, we omit  $\theta$  from Equation 9 in the manuscript.

The light from the metasurface is propagated using the modeled angular spectrum method (ASM) with a parameterized Fourier plane to account for the IRIS placed inside the  $4f$  system and optical aberration. The phase aberration of the plane is modeled using Zernike polynomials up to the 9th order. After the parameterized ASM, the reconstructed amplitude passes through the CNN for image adjustment. Overall, our propagation model can be expressed as follows:

$$f_{\text{model}}(\phi) = \text{CNN}_{\text{target}} \left( f_{\text{ASM}} \left( J_{\text{proxy}}(l, w) \cdot J_{\text{hwp}}(\theta; \theta_{\text{tilt}}) \cdot a_{\text{src}} e^{i\phi_{\text{src}}} e^{i(k * \text{MLP}(\phi))}; a_{\mathcal{F}}, \phi_{\mathcal{F}} \right) \right). \quad (\text{S3})$$

Since Jones matrices of the HWP and the metasurface have polarization-dependent elements, we capture the dataset with polarization diversity by changing the rotation angle  $\theta$  of HWP. Therefore we capture the dataset with 4 different settings: without a metasurface, with the metasurface and  $0^\circ$  HWP, with metasurface and  $22.5^\circ$  HWP, and with metasurface and  $45^\circ$  HWP. We train our model with dataset captured with 2,000 SLM phase patterns generated from stochastic gradient descent method and the alternating direction method of multipliers method [Choi et al., 2021]. We use 5 layers U-Net for  $\text{CNN}_{\text{target}}$  and optimize for 10 epochs with a learning rate of  $5e^{-4}$ .

## S2.2 Optimized model parameters

Figure S7 visualizes the trained physical parameters of our CITL-calibrated model, including the source intensity  $a_{\text{src}}$ , source phase  $\phi_{\text{src}}$ , amplitude  $a_{\mathcal{F}}$  and phase  $\phi_{\mathcal{F}}$  of the Fourier plane, SLM phase mapping through MLP, and SLM pixel crosstalk kernel. Though the phase of the Fourier plane  $\phi_{\mathcal{F}}$  is modeled in a depthwise manner, only the phase of the central plane is showcased in the figure as a representative. Additionally, Figure S8 visualizes the trained polarization-dependent transmission coefficients of the metasurface. The model successfully captures misalignment due to shifts or distortions, as well as additional noise from dust and scratches, along with the fabricated phase patterns. The misaligned angles of the HWP are  $-2.84^\circ$ ,  $-2.00^\circ$ , and  $-1.78^\circ$  for the red, green, and blue channels, respectively. We utilize the CITL-calibrated model for CGH optimization during the experimental validation.

## S3 ADDITIONAL RESULTS

### S3.1 Metasurface optimization result

Figure S9 visualizes the geometric parameters of the metasurface nanostructure. The left figure illustrates the schematic diagram of the metasurface nanostructures. During the metasurface optimization, the height  $H$  and pixel pitch  $P$  are fixed at 800 nm and 283 nm, respectively, while only the geometry maps of length  $L$  and width  $W$  are optimized.

The first column displays the geometry-maps of a random metasurface utilized in the simulations presented in Figure 5 and Figure 6. The geometry-maps of the random metasurface follow a uniform random distribution. The second column showcases a metasurface optimized without the noise function, which is utilized for the simulation in Figure 4. The last column illustrates the optimized metasurface with the noise function, which is actually fabricated for the experiment. The optimized metasurfaces exhibit coarser geometry-map patterns compared to the random metasurface. However, the metasurface without the noise function displays grainy, randomized patterns that make it more vulnerable to misalignment.

The power spectrum of the optimized metasurface can be found in Fig. S10. The power spectrum is derived from the Fourier transform of the complex amplitude of the metasurface. For more clear visualization, we illustrate the power spectrum is displayed on a normalized logarithmic scale. The power spectral distribution is predominantly focused on the DC component, similar to a diffuser with a narrow diffusing angle. This aligns with the interpretation of the metasurface in the manuscript Section 4, which concludes that the metasurface is optimized to have a tailored randomness.

### S3.2 Additional simulation results with partially coherent light sources

Figure S11 showcases simulation results with multiple levels of coherence. Consistent with the simulation in the manuscript, the focal length of the collimating lens is fixed to 200 mm, while we adjust the bandwidth and the aperture width of the light source. We modeled the light source's wavelength spectrum as a Gaussian distribution, with wavelength diversity represented by the standard deviation,  $\sigma$ . During the simulation, we first optimized the SLM phase pattern for a 2D target image using a coherent light source, and reconstructed this phase pattern with variations in the light source. The results show that the image gets blurry as the aperture size and the bandwidth increase, illustrating trade-offs in partially coherent light sources. We note that increased wavelength diversity introduces speckle noise in the image. This is because, while the speckle noise seems absent for the optimized condition in simulation, it reemerges when the reconstruction condition is different from the optimized one. However, in practice, the speckle noise is also inherent in a coherent light source, and increasing wavelength diversity reduces speckle noise at the expense of the image contrast.

### S3.3 Additional simulation and experimental results of depolarized holography

We provide additional simulation results in Figure S12 and experimentally captured results in Figure S13. Both results shows holograms with focal stack supervision. The first column represents the hologram reconstructed without the metasurface, which is equivalent to the conventional holographic displays. Second column shows the case where the metasurface inserted to the display, but only hologram with a single polarization state is captured. Third column is the depolarized holography, where two holograms with orthogonal polarization states are superimposed together as an intensity sum, achieving the best image quality among these three cases. An interesting observation is that even a single polarizer provides better contrast, which was not observed in the simulation. This finding contributes to the optimization of the focal stack hologram CITL. Although the peak signal-to-noise ratio (PSNR) is lower due to speckle noise, the distribution remains similar to that depicted in the histogram represented in manuscript. This indirectly implies that the degree of freedom offered by the polarization channel aids optimization, not solely in speckle reduction.

## REFERENCES

- Amir Arbabi, Yu Horie, Mahmood Bagheri, and Andrei Faraon. 2015. Dielectric metasurfaces for complete control of phase and polarization with subwavelength spatial resolution and high transmission. *Nature Nanotechnology* 10, 11 (2015), 937–943.
- Suyeon Choi, Manu Gopakumar, Yifan Peng, Jonghyun Kim, Matthew O'Toole, and Gordon Wetzstein. 2022. Time-Multiplexed Neural Holography: A Flexible Framework for Holographic Near-Eye Displays with Fast Heavily-Quantized Spatial Light Modulators. In *ACM SIGGRAPH 2022 Conference Proceedings* (Vancouver, BC, Canada) (*SIGGRAPH '22*). Association for Computing Machinery, New York, NY, USA, Article 32, 9 pages.
- Suyeon Choi, Manu Gopakumar, Yifan Peng, Jonghyun Kim, and Gordon Wetzstein. 2021. Neural 3D Holography: Learning Accurate Wave Propagation Models for 3D Holographic Virtual and Augmented Reality Displays. *ACM Trans. Graph.* 40, 6, Article 240 (2021), 12 pages.
- Changwon Jang, Kiseung Bang, Minseok Chae, Byoungcho Lee, and Douglas Lanman. 2022. Waveguide Holography: Towards True 3D Holographic Glasses.
- Changil Kim, Henning Zimmer, Yael Pritch, Alexander Sorkine-Hornung, and Markus H Gross. 2013. Scene reconstruction from high spatio-angular resolution light fields. *ACM Trans. Graph.* 32, 4 (2013), 73–1.
- J. P. Balthasar Mueller, Noah A. Rubin, Robert C. Devlin, Benedikt Groever, and Federico Capasso. 2017. Metasurface Polarization Optics: Independent Phase Control of Arbitrary Orthogonal States of Polarization. *Physical Review Letters* 118, 11 (2017), 113901.
- Yifan Peng, Suyeon Choi, Nitish Padmanaban, and Gordon Wetzstein. 2020. Neural Holography with Camera-in-the-Loop Training. *ACM Trans. Graph.* 39, 6, Article 185 (nov 2020), 14 pages.

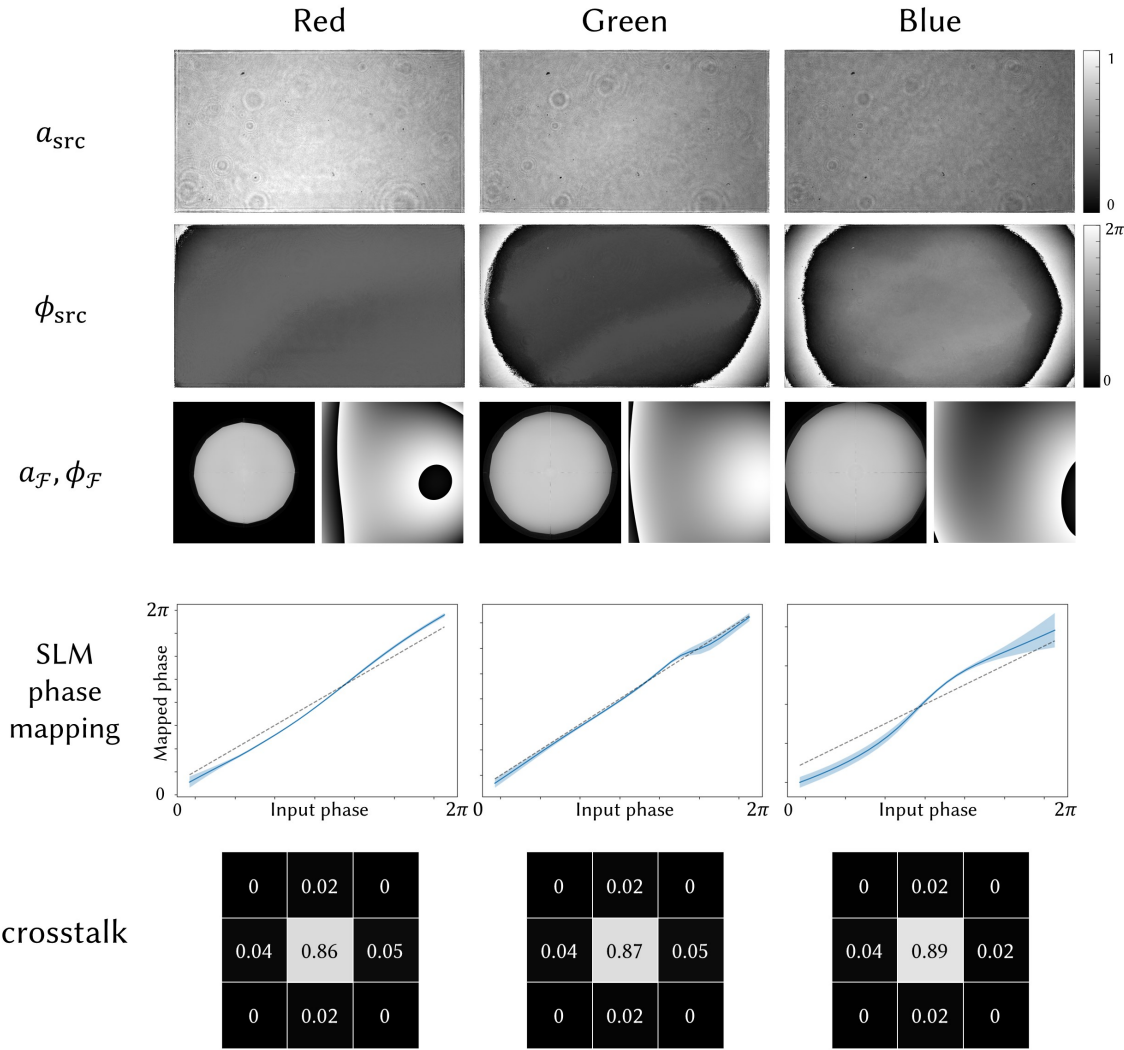


Fig. S7. Visualization of the physical parameters in the CITL-calibrated model, excluding the metasurface and HWP. In the SLM phase mapping, the dashed lines indicate the ideal mapping, while the blue solid line represents the average of the mapped phase values. The blue shaded region indicates the standard deviation. Additionally, the 3x3 crosstalk kernels are depicted in an enlarged format, with the numbers in each pixel representing the weight of the kernel.

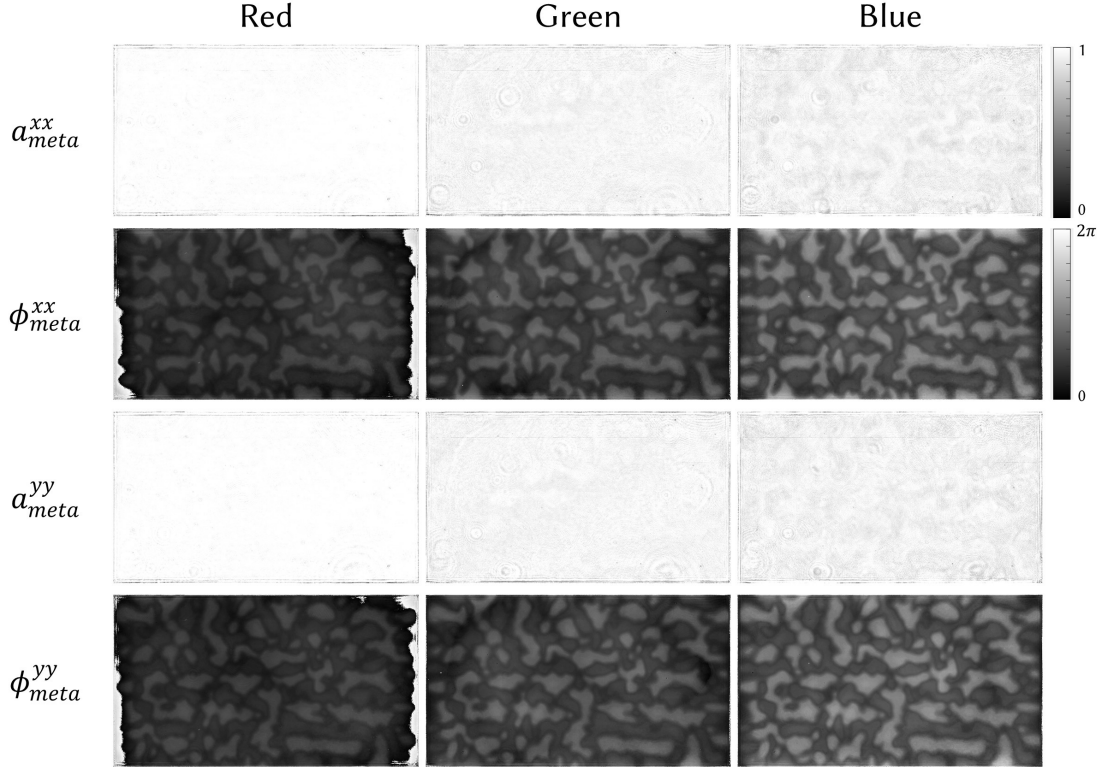


Fig. S8. Visualization of the trained amplitude and phase of the metasurface in the CITL-calibrated model. Both the phase and amplitude patterns are consistent with the ideal ones derived from the geometry-maps shown in Figure S9. The trained metasurface also includes the effects of defects from dust and scratches, as well as phase fluctuations due to the glass substrate.

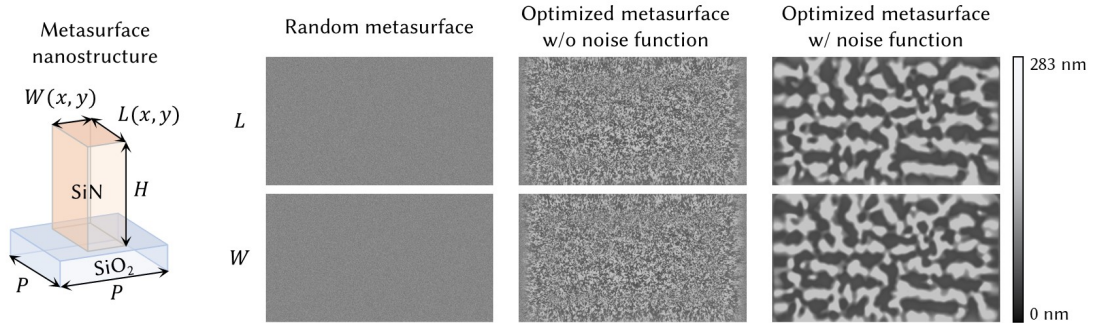


Fig. S9. (left) The schematic diagram of the metasurface nanostructure. The pixel pitch  $P$ , height  $H$ , length  $L$ , and width  $W$  determine the transmittance of the metasurface. (right) The geometry-maps of the metasurfaces used in simulations and experiments. The dimensions of length  $L$  and width  $W$  are normalized with respect to the 283 nm pixel pitch

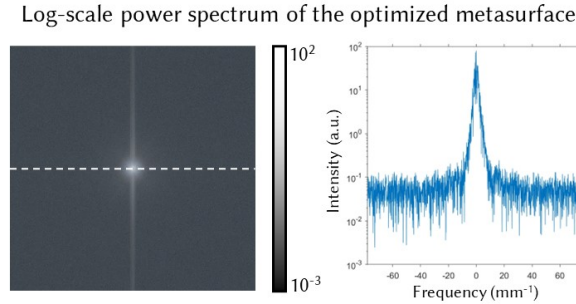


Fig. S10. Power spectral distribution of the optimized metasurface. For clarity in visualization, the power spectrum is displayed in a logarithmic scale and normalized. The plot on the right shows the cross-section of green channel from the 2D power spectrum, indicated by the white dashed line.

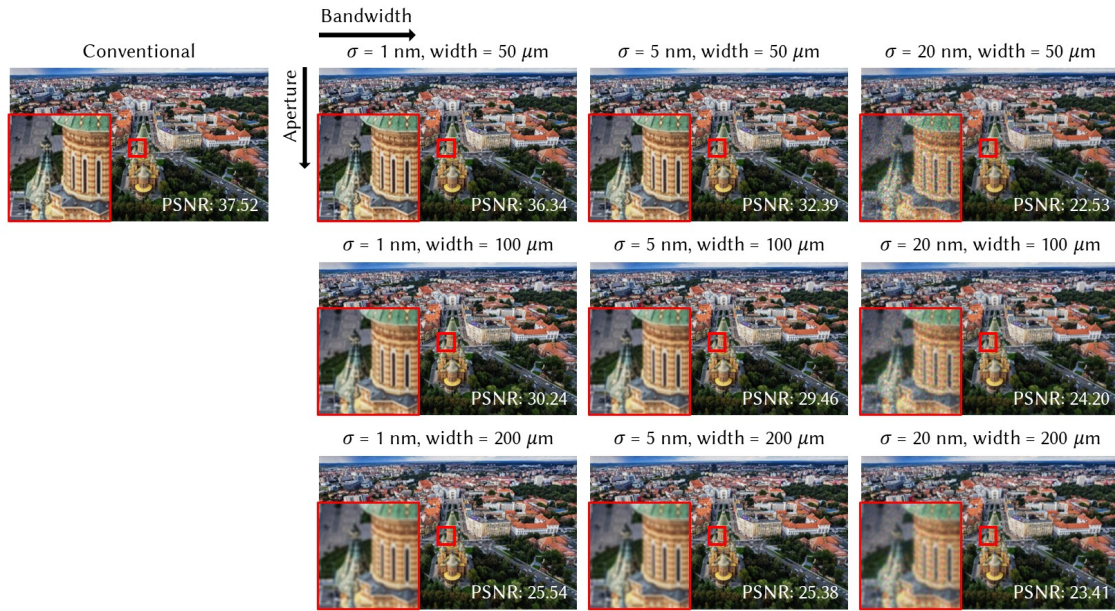


Fig. S11. Simulation results with multiple levels of coherence. The same SLM phase pattern, optimized for a coherent light source, is applied for all images simulated with different light sources. The results shows trade-offs between image contrast and speckle reduction in partially coherent light sources. Source image credits to Salomia Oana Irina.



Fig. S12. Simulation results of holograms with focal stack supervision. PSNR values are reported at the bottom right corner of the image. Source images credit to BAZA Production (first row), Salomia Oana Irina (second row), and Kim et al. [2013] (third row).

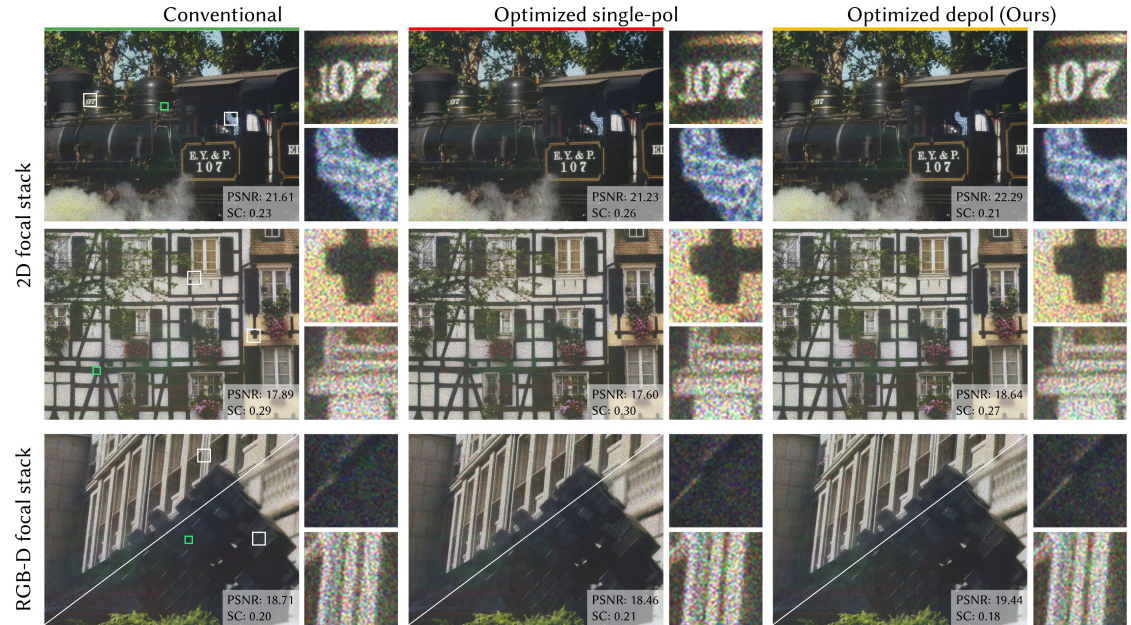


Fig. S13. Experimentally captured images of holograms with focal stack supervision. PSNR and speckle contrast values are reported at the bottom right corner of the image. The green box specifies the area that the speckle contrast is calculated. Source images credit to Bruce Raynor (first row), Pack-Shot (second row), and Kim et al. [2013] (third row).